

Elastic and magnetoelastic properties of TbMnO₃ single crystal by nanosecond time resolved acoustics and first-principles calculations

P. Hemme¹, C-H. Li^{2,3}, P. Djemia², P. Rovillain⁴, S. Houver¹, Y. Gallais¹, A. Sacuto¹, H. Sakata⁵, S. Nowak⁶, B. Baptiste⁷, E. Charron⁴, B. Perrin⁴, L. Belliard⁴, and M. Cazayous^{1*}

¹Laboratoire Matériaux et Phénomènes Quantiques,

Université de Paris, UMR 7162 CNRS, 75205 Paris Cedex 13, France

²Laboratoire des Sciences des Procédés et des Matériaux UPR-CNRS 3407,

Université Sorbonne Paris Nord, Alliance Sorbonne Paris Cité, Villetaneuse, 93430, France

³School of Materials Science and Engineering, Beijing Institute of Technology, Beijing, 100081, China

⁴Institut des Nanosciences de Paris, Sorbonne Université,

CNRS UMR 7588, 4 place Jussieu, 75005 Paris, France

⁵Department of Physics, Tokyo University of Science,

1-3 Kagurazaka Shinjyuku-ku Tokyo, Japan 162-8601

⁶UFR de Chimie, Université de Paris, 15 rue Jean Antoine de Baïf, 75013 Paris, France

⁷Institut de Minéralogie, de Physique des Matériaux et de Cosmochimie,

CNRS UMR 7590, Sorbonne Université, 75005 Paris, France

Time resolved pump and probe acoustics and first-principles calculations were employed to assess elastic properties of the TbMnO₃ perovskite manganite having orthorhombic symmetry. Measuring sound velocities of bulk longitudinal and shear acoustic waves propagating along at least two different directions in the high symmetry planes (100), (010) and (001), provided a powerful mean to selectively determine the six diagonal elastic constants $C_{11}=227$ GPa, $C_{22}=349$ GPa, $C_{33}=274$ GPa, $C_{44}=71$ GPa, $C_{55}=57$ GPa, $C_{66}=62$ GPa. Among the three remaining off-diagonal ones, $C_{23}=103$ GPa was determined with a bissectrice direction. Density functional theory calculations with colinear spin-polarized provided complementary insights on their optical, elastic and magnetoelastic properties.

Multiferroics are well known materials that display simultaneously ferroelectric and magnetic properties.¹ Beside their exciting physics, strong magnetoelectric coupling, present in some of them, has opened up a whole field of applications for new spin-based devices^{2,3}. Several multiferroics own an original process to induce ferroelectricity from a magnetic state, the so-called improper multiferroics such as the perovskite manganites TbMnO₃.⁴ The ferroelectricity in TbMnO₃ has its origin from the magnetic exchange striction^{5,6} or from a spin order breaking the spatial inversion symmetry via the spin-orbit interaction.⁷⁻¹⁰ The novel couplings between microscopic degrees of freedom such as spin and charge is the main reason why TbMnO₃ is one of the most intensively investigated magnetoelectric manganite among the frustrated magnets. The strength of the magnetoelectric coupling gives rise to unusual dynamical effects like electromagnons, spin waves that are excited by the electric-field component of light¹¹⁻¹⁵. One of the two electromagnons observed in TbMnO₃ has already been explained as a zone-edge magnon activated purely by the magnetostriction mechanism.^{14,16,17} Yet, the multiferroic properties of these compounds exist only at very low temperature with a weak polarization, which limits application perspectives. However, a possible start of application has been demonstrated using electromagnons to modify the atomic-scale magnetic structure of TbMnO₃ with THz optical pulses¹⁸. In addition, strain engineering has emerged as a powerful means for tuning the multiferroic mechanisms of perovskite oxide thin films.¹⁹ The determination of the magnetostriction and magnetoelas-

tic coefficients, and consequently the knowledge of the elastic coefficients are essential to be able to quantify the interactions that are at work in these complex couplings. To the best of our knowledge, there is no experimental determination of the TbMnO₃ elastic coefficients. The few works on the subject are theoretical,²⁰ one employing a shell model with transferable pairwise interionic interaction potential.²¹ In order to remedy this shortcoming, we applied the pump-probe time-resolved acoustics method we recently developed for the rhombohedral multiferroic BiFeO₃²² to TbMnO₃ which has 9 independent elastic constants. This approach has been extended to the magnetoelastic properties which knowledge is crucial for this type of compound.

In this work, sound velocities of both longitudinal and transverse acoustic modes traveling along different directions in single crystals TbMnO₃ have been measured using an acoustical pump-probe experiment at the nanosecond time-scale. To date, no other experimental technique allows to do this on a material of which only small samples exist. To meet the challenge of performing a successful analysis of these data to identify the maximum of elastic constants, we used the Christoffel equation and elastic constants calculated by the density functional theory (DFT). We have been able to determine a set of initial theoretical velocities. Then, among all nine independent C_{ij} elastic constants of TbMnO₃, seven have been selectively measured along high symmetry directions of the lattice. In addition, we have tracked unambiguously each acoustic wave by identifying simultaneously their sound velocities and their different polarizations. Lastly,

the anisotropic magnetostriction and magnetoelastic coefficients of TbMnO_3 has been simulated by DFT and compared to the calculated ones of BiFeO_3 .

We have investigated three different planes [b, c], [a, c] and [a, b] of highest symmetry, all oriented from the same TbMnO_3 single crystal grown by floating-zone method. TbMnO_3 becomes antiferromagnetic below the Néel temperature $T_N=42$ K.²³ In this phase the Mn magnetic moments form an incommensurate sinusoidal wave with a modulation vector along the b axis. The ferroelectric order appears below $T_C=28$ K at the magnetic transition from incommensurate to commensurate order where the spin modulation becomes a cycloid.²⁴ The crystal axes and the lattice parameters have been determined for each samples using a X-ray diffractometer with a 4-axis goniometer. TbMnO_3 crystallizes in the orthorhombic symmetry ($Pnma$) with lattice parameters equal to $a = 5.833 \pm 0.080$ Å, $b = 7.429 \pm 0.050$ Å, $c = 5.301 \pm 0.050$ Å and a mass density $\rho=7.51 \pm 0.2$ g/cm³. They compare well to reported values $a = 5.838$ Å, $b = 7.402$ Å, $c = 5.293$ Å with a mass density $\rho=7.603$ g/cm³.²⁵ The crystals have been polished and an aluminium thin film of 75 nm has been evaporated on the surface. For our pump and probe optical method, the Al allows to enhance the acoustic waves generated in TbMnO_3 by the pump and the reflectivity signal from the surface displacements detected by the probe. The thickness of Al is very small compared to the wavelengths of the acoustic waves involved in our experiment, and therefore should not disturb significantly the dispersion curves of acoustic waves and the propagation speeds.

Acoustical pump-probe method has been implemented to measure sound velocity within the plane of three differently oriented single crystals (100), (001) and (010), and thus to determine elastic constants. The source is a mode-locked Ti:sapphire. The pump-probe time-delayed is tuned using a mobile reflector with a maximum amplitude of 12 ns. The surface displacements are measured by a Michelson interferometer detecting the phase of the reflectivity changes. A more detailed description of our pump-probe experiment can be found in the supplementary material and in previous works.²⁶⁻²⁸

Figures 5 (a, b, c) show the propagation of the acoustic waves on the (100), (001) and (010) TbMnO_3 surface, respectively. The signal is recorded by scanning the surface of the sample ($28 \times 28 \mu\text{m}^2$) at fixed pump-probe delay. It corresponds to a snapshot taken after 3 ns from the coincidence (temporal overlap of the pump and probe). The black area in the center of the image is from photothermal stationary component while the contrast in intensity corresponds to maxima and minima in the amplitude of the wavefront. For the present time- and length-scale, we see only in Fig. 5 one wavefront with an elliptic shape for each planes identified later as a shear vertical wave.

Hence, we have performed scan lines along at least two directions exhibiting highest and lowest propagating sound velocities. Profiles of the acoustic waves at different times of probe arrival after the coincidence, from

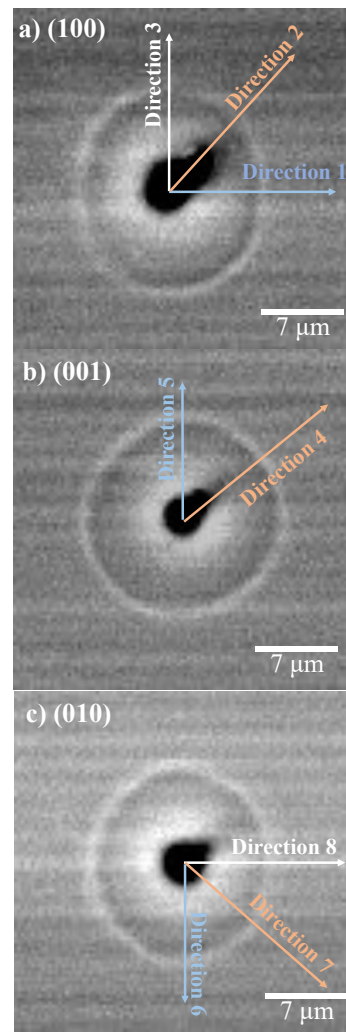


FIG. 1: Scan of the TbMnO_3 ($Pnma$ frame reference) (a) (100), (b) (001) and (c) (010) surfaces at a fixed pump-probe delay of 3 ns showing the propagating acoustic waves (here shear ones only) emerging from the epicenter. The studied directions have been drawn.

2 ns to 4 ns by step of 200 ps are shown in Figs. 2(a, b, c). They present the relative change of phase of the probe reflectivity along the scanned "direction 2", "direction 5" and "direction 7" on (100), (001) and (010) plane, respectively, as a function of the probe position on the sample, along the given direction. One can observe in Figs. 2, either, one or two peaks (see the supplementary material, the second peak is associated to a second wavefront not observable in Fig. 5) whose positions evolve as a function of the probe delay time, the first one being always much more intense. These peaks correspond to wave amplitude maxima and distinct propagation speeds, the first peak being the slowest one. For seek of simplicity, analysis will first consider bulk acoustic waves and later surface acoustic waves, all remaining close to each other. Our measurements are performed on

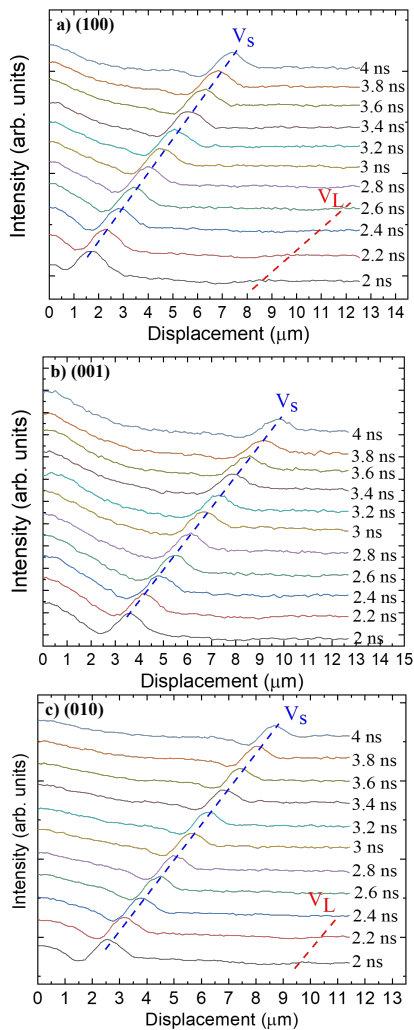


FIG. 2: Relative phase change of the electromagnetic field of the probe beam as a function of the displacement and at different probe time delay, along analyzed directions: (a) "2", (b) "5" and (c) "7".

(100), (001) and (010) planes, the three high symmetry planes of the orthorhombic crystal. In these planes, one longitudinal (L) and one shear (S1) acoustic waves are polarized and propagating parallel to the plane, and the second shear wave (S2) has polarization perpendicular to the plane (see description in the supplementary material). In total, eight directions were investigated, from which exact attribution and description of these peaks (Fig.2) could be performed thanks to analytical relations described in the supplementary material and are reported in Table I. In one plane, maximum and minimum sound velocity is necessarily along one high symmetry direction x_i ($i=1..3$). The appearance of one common direction on each plane with similar sound velocity was considered, and helped us to identify highest symmetry directions x_1 , x_2 and x_3 .

In order to attribute the measured sound velocities to

Label	Velocity (L or S)	Direction(plane)	Elastic constants
1	(L) 5150 ± 300	[010](100)	C_{22}
1	(S) 2733 ± 22	[010](100)	C_{66} or C_{44}
2	(L) 5359 ± 82	[011](100)	$C_{b+c,L}$
2	(S) 2820 ± 16	[011](100)	$\frac{C_{66}+C_{55}}{2}$ or $C_{b+c,S1}$
3	(L) 4911 ± 38	[001](100)	C_{33}
3	(S) 2861 ± 38	[001](100)	C_{55} or C_{44}
4	(S) 2933 ± 20	[110](001)	$\frac{C_{55}+C_{44}}{2}$ or $C_{a+b,S1}$
5	(S) 3070 ± 15	[010](001)	C_{44} or C_{66}
6	(S) 3114 ± 13	$[\bar{1}01](010)$	$\frac{C_{66}+C_{44}}{2}$ or $C_{a+c,S1}$
7	(L) 4841 ± 150	[001](010)	C_{33}
7	(S) 3044 ± 17	[001](010)	C_{44} or C_{55}
8	(S) 2947 ± 23	$[10\bar{1}](010)$	$\frac{C_{66}+C_{44}}{2}$ or $C_{a+c,S1}$

TABLE I: Measured sound velocities (V) along the analyzed directions labelled (1-8), identified crystallographic directions and relations with the $C_{ij} = \rho V^2$ elastic constants. V_L and V_S are the longitudinal and shear sound velocities given in m/s. C_{ij} is related to the shear wave (S2) with a vertical (out-of-plane) polarization.

$$C_{b+c,L} = \frac{C_{22} + C_{33} + 2C_{44}}{4} + \frac{1}{2} \sqrt{\frac{(C_{33} - C_{22})^2 + 4(C_{44} + C_{23})^2}{4}}$$

$$C_{b+c,S1} = \frac{C_{22} + C_{33} + 2C_{44}}{4} - \frac{1}{2} \sqrt{\frac{(C_{33} - C_{22})^2 + 4(C_{44} + C_{23})^2}{4}}$$

$$C_{a+c,S1} = \frac{C_{11} + C_{33} + 2C_{55}}{4} - \frac{1}{2} \sqrt{\frac{(C_{33} - C_{11})^2 + 4(C_{55} + C_{13})^2}{4}}$$

$$C_{a+b,S1} = \frac{C_{11} + C_{22} + 2C_{66}}{4} - \frac{1}{2} \sqrt{\frac{(C_{22} - C_{11})^2 + 4(C_{66} + C_{12})^2}{4}}$$

the correct acoustic modes, we have implemented several calculation steps to optimize the elastic constants by minimizing the difference between the experimental and analytical theoretical velocities. Knowing the C_{ij} elastic constants and mass density (we used $\rho = 7603 \text{ kg/m}^3$) of the material, allows to calculate sound velocities by solving the Christoffel equation (section A in the supplementary material for any direction in (100), section B for the (010) plane and section C for the (001) plane). According to the TbMnO_3 space-group symmetry (Pnma), the elastic constant tensor C_{ij} has nine independent constants,²⁹ namely, C_{11} , C_{12} , C_{13} , C_{22} , C_{23} , C_{33} , C_{44} , C_{55} and C_{66} , sufficient to simulate any other elastic properties. For ab initio calculations, we first followed a similar strategy than our previous work on BFO²². Electronic-structure calculations are carried out using a plane-wave pseudopotential approach to DFT as implemented within the VASP code^{30,31} using the electron-ion interaction, described via the projector augmented wave method and potentials^{32,33}. We considered a collinear-spin magnetization type with generalized gradient approximation (GGA), to depict the exchange correlation functional. We used both the Perdew–Burke–Ernzerhof (PBE) and the one revised for solids (PBEsol)³⁴ to vary the equilibrium atomic volume at which the elastic properties are determined, with on-site Coulomb interactions (GGA+U). In this simplified approach of Dudarev *et al.*³⁵, we let Hubbard effective parameter U to vary between 0 and 7 eV to search for the band gap close to the experimental value of 0.5 eV,³⁶ and spanning a large range of equi-

librium volume and lattice parameters. This is a spin-polarized magnetic calculation, with electronic iterations convergence of 0.0001 meV using the Normal (blocked Davidson) algorithm, plane wave cutoff energy of 520 eV and reciprocal space projection operators. The Brillouin-zone k -mesh is forced to be centered on the gamma point and corresponds to actual k -spacings of $6 \times 5 \times 6$. The stress-strain method as implemented in VASP is employed (VASP-TAG IBRION=6), and elastic constants are determined on the relaxed structures by using the tetrahedron method incorporating Blöchl corrections.³⁷

Due to approximations in the DFT+U method, we cannot directly compare energetics (total energy E_t) at different values of U . However we can compare energies that have been referenced to a common value, for example the ground state defined by the cell volume $V_0(U)$ and the lowest total energy $E_0(U)$, obtained for each U value. Rather than using this representation ($E_{real}=E_t-E_0$) versus the volume for the two flavor of exchange functional (GGA-PBE and GGA-PBESol), we kept the modification of the ground state atomic volume versus U , as shown in Fig.3. It has the advantage to clearly show that GGA-PBESol + U is approaching the experimental value $V_0 \approx 57.19-57.43 \text{ \AA}^3$ for $U \approx 7 \text{ eV}$. The dynamical stability has been evaluated thanks to the phonon spectrum in the supplemental material.

All nine C_{ij} values calculated by DFT are reported in Table II. While GGA-PBE is always overestimating, closer values of lattice parameters and cell volume are found for GGA-PBESol with $U=7 \text{ eV}$, while band gap is 0.529 eV. Then, first comparison with experimental sound velocities and elastic constants can be done with those obtained by this GGA-PBESol+ $U=7 \text{ eV}$ functional, referred later as "DFT" values.

Here are examples to illustrate our approach. We measured very closed sound velocity of L-wave (4911 and 4841 m/s) along direction x_2 in both (100) and (001) planes, as well as, very closed sound velocity of S-wave (3070 and 3044 m/s) along direction x_3 (direction 5) and x_2 (direction 7), in both (001) and (010) planes. The sound velocity of L-wave is associated to the C_{22} elastic constant. Remember that our interferometric detection scheme favours the observation of shear wave (S2) having vertical out-of-plane component polarization. The C_{44} elastic constant is thus associated to the sound velocity of S-wave. The C_{66} , C_{55} and C_{33} were determined with a second direction in the (100) plane. C_{44} agrees very well with DFT one, while other measured elastic constants are below by 15-40%.

The determination of the remaining diagonal elastic constant C_{11} need a second independent measurement of C_{22} and C_{33} . Both constants were determined by a complementary time domain Brillouin scattering (TDBS) experiment (see the supplementary material) which measured the product of refractive index by the longitudinal sound velocity (nV_L) traveling along the normal of sample plane. This experiment allows mainly a study

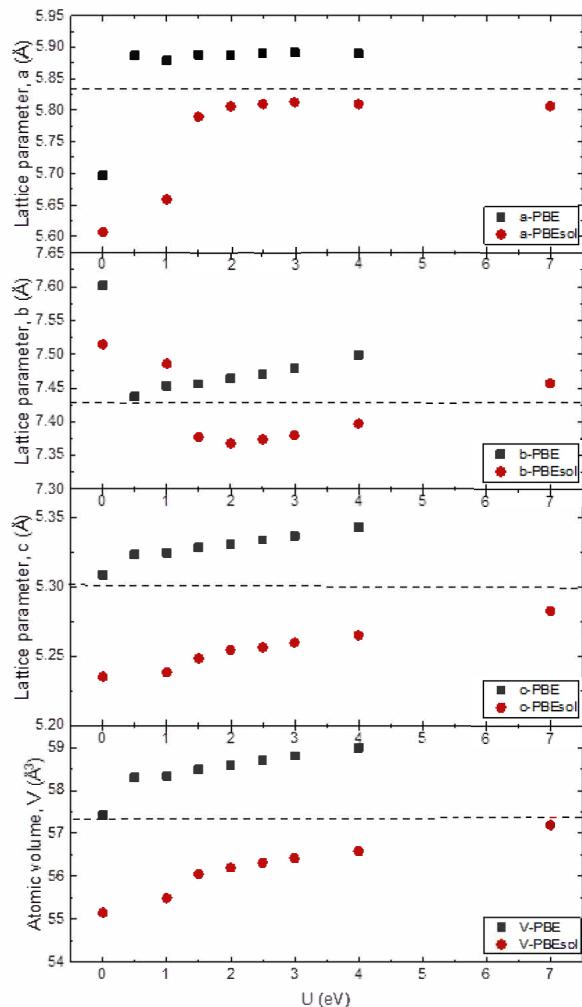


FIG. 3: Lattice parameter and atomic volume calculated by GGA-PBE and GGA-PBESol as a function of the effective Hubbard U term. Our experimental values are shown by a dashed-line.

of out-of-plane modes compared to the acoustical pump-probe method which allows to probe mainly the in-plane modes. We calculated the anisotropic refractive index n ($n_a=2.16$ and $n_c=2.24$) at a wavelength of $\approx 800 \text{ nm}$ (photon energy 1.5 eV) to serve as one input for analyzing the results (nV_L) of TDBS experiments^{39,40} conducted for each planes. To do so, we performed additional DFT calculations with the hybrid functional (Heyd-Scuseria-Ernzerho, HSE06)⁴¹⁻⁴³ as implemented in VASP. The frequency-dependent optical properties are calculated using the VASP-TAG (LOPTICS=.TRUE.) and the complex shift used to smoothen the real part of the dielectric function is set to 0.1. Here we use the only one available experimental value of refractive index ($n_c=2.35$) measured at 30K,⁴ nearly 10% higher than our DFT ones.

The measured longitudinal sound velocities measured

	DFT ^a	DFT ^b	Theo. ³⁸	Exp. ²⁵	Exp. final set ^c
C ₁₁	185-209	174-249	170	-	-
C ₁₂	131-147	141-173	-	-	-
C ₁₃	93-117	109-118	-	-	-
C ₂₂	255-277	268-301	150	-	202±20
C ₂₃	110-128	121-144	-	-	103±6
C ₃₃	239-257	265-275	197	-	181±2
C ₄₄	87-91	43-76	48	-	71±5
C ₅₅	50-77	75-83	73	-	60±2
C ₆₆	62-75	100-101	77	-	61±4
V ₀	58.0-59.1	55.5-57.19	56.5	57.19	57.43±0.19
a	5.7-5.9	5.6-5.81	5.817	5.8384	5.83±0.08
b	7.46-7.61	7.46-7.51	7.438	7.4025	7.43±0.05
c	5.34	5.23-5.28	5.228	5.2931	5.30±0.05

TABLE II: C_{ij} elastic constants determined in this work by DFT with GGA-PBE^a+U and GGA-PBESol^b+U exchange-correlation functional and on-site Coulomb interaction (U = 0-7 eV) simplified approach of Dudarev *et al.*³⁵ and our experiments.^c Comparison to values calculated by interatomic shell model²⁰ and x-ray diffraction for lattice parameters.²⁵ Elastic constants values are given in GPa, the equilibrium lattice parameters (a, b and c) in Å and atomic volume V₀ in Å³/atom. Notice that DFT+U has an impact on elastic properties through the ground state volume modification when varying U.

by TDBS and the deduced C₁₁, C₂₂ and C₃₃ elastic constants ($C = \rho V^2$) are reported in Table III. They show a reasonable agreement within 10%, 25% and 3% with DFT ones from Table II, respectively (for a discussion of the agreement see the supplementary material). Notice that the TDBS measurements do not show transverse waves in TbMnO₃ contrary to the multiferroic BiFeO₃ compound^{22,45} which remains a special case.

V_L (m/s)	Direction	Elastic constant (GPa)
5468±110	[100]	C ₁₁ =227±10
6780±134	[010]	C ₂₂ =349±17
6002±120	[001]	C ₃₃ =274±10

TABLE III: Longitudinal sound velocity (V_L) and elastic constants (C_{ii}) determined in this work by TDBS along the normal of each plane samples by TDBS. A common refractive index $n_b=2.35$ (photon energy, 1.5 eV) measured at 30K by Trepakov *et al.*⁴ is used.

To push further the analysis, we performed the calculations of surface acoustic waves sound velocities which can propagate in each three high symmetry planes, considering the following set of elastic constants: C₁₁= 227 GPa, C₂₂= 349 GPa, C₃₃= 274 GPa, C₄₄= 71 GPa, C₅₅= 57 GPa, C₆₆= 62 GPa, C₁₂= 141 GPa, C₁₃= 109 GPa, C₂₃= 103 GPa,²² and compared them to the bulk ones in Fig. 4.

Figure 4 shows the calculated and measured acoustic waves sound velocities on the (a) (100), (b) (001) and (c) (010) surfaces. We clearly see in this figure, first,

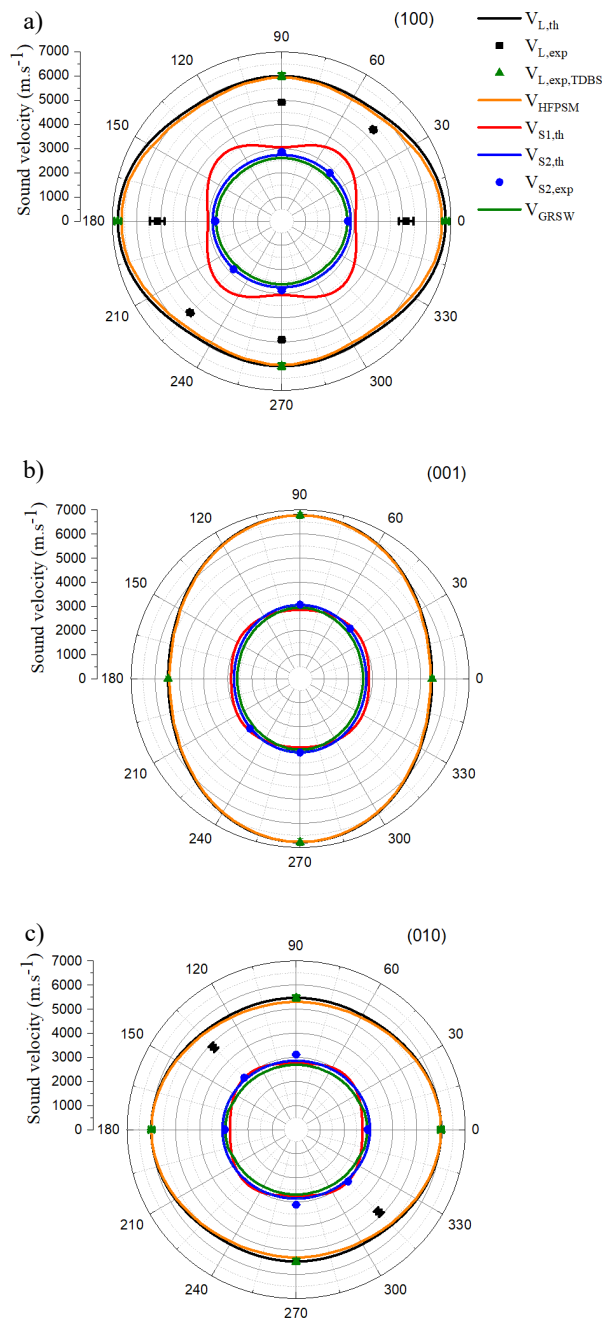


FIG. 4: Comparison of the TbMnO₃ (Pnma frame reference) (a) (100), (b) (010) and (c) (001) surfaces between experimental and simulated data.

the elliptical shape as in Fig.5 and that the generalized Rayleigh surface acoustic wave (GRSW) with the lowest velocity remains very close to the bulk vertical shear wave (S_2) for all directions. The same observation is valid for the high frequency pseudo surface wave (HFPSW) and bulk longitudinal wave (L). This is a validation of our simplified approach with analytical expressions offered in

case of bulk waves we used for the data treatment. However, for the in-plane measurements, we can't conclude on the nature of the wave, bulk or surface waves.

Notice that because it is not obvious to determine what kind of acoustic waves is propagating without any a priori knowledge of their sound velocity and polarization, we have performed preliminary DFT theoretical estimates to guide the identification. This helped us to distinguish between the faster (≈ 5000 m/s) longitudinal wave (L) and the two transverse waves (S1 and S2) propagating with a lower velocity (≈ 3000 m/s), by considering first the range of their respective sound velocity. In a second step, due to our detection schema, we privileged the observation of the only transverse wave having a vertical component (S2).

Magnetostriction/Magnetoelastic coefficients			
TbMnO ₃	TbMnO ₃ x10 ⁻⁶ (MPa)	BiFeO ₃	BiFeO ₃ x10 ⁻⁶ /no coeff.(MPa)
λ_1/b_1	-1.33/0.3	$\lambda^{\alpha 1,2}/b_{21}$	-34.40/6.52
λ_2/b_2	-9.97/0.4	$\lambda^{\alpha 2,2}/b_{22}$	61.94/-3.99
λ_3/b_3	-1.87/0.4	$\lambda^{\gamma,1}/b_3$	58.36/-4.72
λ_4/b_4	18.56/2.9	$\lambda^{\gamma,2}/b_4$	62.26/3.91
λ_5/b_5	2.46/0.3	$\lambda^{1,2}/b_{14}$	0.81/-5.86
λ_6/b_6	-5.27/0.2	$\lambda^{2,1}/b_{34}$	-81.96/0.69
λ_7/b_7	-3.03/1.8		
λ_8/b_8	0.25/0.008		
λ_9/b_9	2.62/0.2		

TABLE IV: The nine anisotropic magnetostriction/magnetoelastic coefficients of TbMnO₃ labelled λ_i/b_i ($i= 1..9$, using the convention in Ref. 46) calculated by DFT (GGA-PBEsol+U= 7eV) in the spin-polarized colinear case. We compare to ones of BiFeO₃ belonging to space group (R3c), we calculated in the same conditions (GGA-PBEsol) as in our previous work [Ref. 22].

As mentioned in the introduction, the determination of the magnetostriction and magnetoelastic coefficients are important to be able to quantify the interactions that give rise to rare phenomena and excitations observed in TbMnO₃. Let's just remember that the degree of magnetostriction can be measured by the magnetostriction coefficient λ , which is the ratio of the fractional change in length (also known as strain or the change in length divided by the original length) to the magnetization of the material. Magnetostriction and magnetoelastic coefficients are directly related to each other by elastic constants. We calculated the nine anisotropic magnetostriction and magnetoelastic coefficients labelled, respectively, λ_i and b_i ($i= 1..9$, respecting the convention in Ref. 46) using the scripts from MAELAS code⁴⁷ and reported in Table IV. These coefficients have been calculated in the colinear spin phase of TbMnO₃.

These calculated values of the magnetostriction parameters could not be compared due to the lack of experimental data measured under the conditions of our calculations. In Ref. 48, magnetostrictive properties have been calculated at 0 K for a different magnetic state compared to the one considered here. We have chosen to compare the magnetostrictive and magnetoelastic constants of TbMnO₃ to the ones of the BiFeO₃ (BFO) material. BFO is very well-known multiferroic compound with amazing properties (conductive domain walls, low bandgap unlike usual ferroelectrics, spectacular THz electromagnetic wave generation). Even for this very studied compound the magnetostrictive and magnetoelastic constants are not well determined. Using the same scripts as the one used for TbMnO₃, the 6 anisotropic magnetostriction and magnetoelastic coefficients of BFO are reported in Table IV. The magnetostriction values of TbMnO₃ obviously do not make this compound suitable for this type of applications. However, in motor shielding, electric transformers or magnetic recording, magnetic materials with extremely small magnetostrictive coefficients are useful. On the contrary, BFO presents large magnetostrictive coefficients needed for many applications in electromagnetic microdevices as actuators and sensors. Our calculated values will serve as a guide to the design or analysis of future experimental works.

In conclusion, acoustical pump-probe experiment at the nanosecond time-scale have been implemented to measure sound velocities of acoustic modes in single crystals TbMnO₃. Among the nine independent C_{ij} elastic constants, seven have been determined. In addition, anisotropic magnetostriction and magnetoelastic coefficients has been simulated by DFT.

SUPPLEMENTARY MATERIAL

See supplementary material for the equations connecting the sound velocities of bulk waves propagating within the three high symmetry planes, to the C_{ij} elastic constants. Complementary results obtained by time domain Brillouin scattering along each high symmetry directions [100] are also provided.

ACKNOWLEDGMENTS

The authors acknowledge J. Rastikian and S. Suffit for the evaporation of aluminium thin film on the TbMnO₃ surface at the cleanroom of Université de Paris.

* corresponding author : maximilien.cazayous@u-paris.fr

¹ Eerenstein W, Mathur N D and Scott J F 2006 *Nature* **442**

759

² Béa H, Gajek M, Bibes M and Barthélémy A 2008 *J.Phys.:*

- Cond. Mat.* **20** 434221
- ³ Spaldin N A and Ramesh R 2019 *Nat. Mat.* **18** 203
- ⁴ Khomskii D 2009 *Physics* **2** 20
- ⁵ Sergienko I A, Sen C and Dagotto E 2006 *Phys. Rev. Lett.* **97** 227204
- ⁶ Picozzi S, Yamauchi K, Sanyal B, Sergienko I A and Dagotto E 2007 *Phys. Rev. Lett.* **99** 227201
- ⁷ Kenzelmann M, *et al.* 2005 *Phys. Rev. Lett.* **95** 087206
- ⁸ Mostovoy M 2006 *Phys. Rev. Lett.* **96** 067601
- ⁹ Hu J 2008 *Phys. Rev. Lett.* **100** 077202
- ¹⁰ Mochizuki M and Furukawa N, 2009 *Phys. Rev. B* **80** 134416
- ¹¹ Pimenov A, Mukhin A A, Ivanov V Y, Travkin V D, Balbashov A M and Loidl A 2006 *Nat. Phys.* **2** 97
- ¹² Senff D, *et al.* 2007 *Phys. Rev. Lett.* **98** 13720
- ¹³ Takahashi Y, *et al.* 2008 *Phys. Rev. Lett.* **101** 187201
- ¹⁴ Valdés Aguilar R, Mostovoy M, Sushkov A B, Zhang C L, Choi Y J, Cheong S W and Drew H D 2009 *Phys. Rev. Lett.* **102** 047203
- ¹⁵ Rovillain P, Cazayous M, Gallais Y, Sacuto A, Measson M-A, and Sakata H 2010 *Phys. Rev. B* **81** 054428
- ¹⁶ Stenberg P V and De Sousa R 2009 *Phys. Rev. B* **80** 094419
- ¹⁷ Mochizuki M, Furukawa N and Nagaosa N 2010 *Phys. Rev. Lett.* **104** 177206
- ¹⁸ Kubacka T, *et al.* 2014 *Science* **343** 1333
- ¹⁹ Shimamoto K, *et al.* 2017 *Scientific Reports* **7** 44753
- ²⁰ Choithrani R, Rao M N, Chaplot S L, Gaur N K and Singh R K 2011 *J. Magn. Magn. Mater.* **323** 1627
- ²¹ Choithrani R, Rao M N, Chaplot S L, Gaur N K and Singh R K 2009 *New J. Phys.* **11** 073041
- ²² Hemme P, *et al.* 2021 *Appl. Phys. Lett.* **118** 062902
- ²³ Quezel S, Tcheou F, Rossat-Mignod J, Quezel G and Roudaut E 1977 *Physica* **86** 916
- ²⁴ Kimura T, Goto T, Shintani H, Ishizaka K, Arima T and Tokura Y 2003 *Nature* **426** 55
- ²⁵ Alonso J A, Martínez-Lope M J, Casais M T and Fernández-Díaz M T 2000 *Inorg. Chem.* **39** 917
- ²⁶ Belliard L, Huynh A, Perrin B, Michel A, Abadias G and Jaouen C 2009 *Phys. Rev. B* **80** 155424
- ²⁷ Amziane A, Belliard L, Decremps F and Perrin B 2011 *Phys. Rev. B* **83** 014102
- ²⁸ Xu F, Belliard L, Fournier D, Charron E, Duquesne J-Y, Martin S, Secouard C and Perrin B 2013 *Thin Solid Films* **548** 366
- ²⁹ Born M, and Huang K 1988 *Dynamical Theory of Crystal Lattices* Oxford University Press, New York
- ³⁰ Kresse G and Furthmüller F 1996 *Comput. Mater. Sci.* **366** 15
- ³¹ Kresse G and Furthmüller F 1996 *Phys. Rev. B* **54** 11169
- ³² Blöchl P E 1994 *Phys. Rev. B* **50** 17953
- ³³ Kresse G and Joubert D 1999 *Phys. Rev. B* **59** 1758
- ³⁴ Perdew J P, Ruzsinszky A, Csonka G I, Vydrov O A, Scuseria G E, Constantin L A, Zhou X and Burke K 2008 *Phys. Rev. Lett.* **100** 136406
- ³⁵ Dudarev S L, Botton G A, Savrasov S Y, Humphreys C J and Sutton A P 1998 *B* **57** 1505
- ³⁶ Cui Y, Wang C and Cao B 2005 *Solid State Com.* **133** 641
- ³⁷ Blöchl P E, Jepsen O and Andersen O K 1994 *Phys. Rev. B, Condensed matter* **49** 16223
- ³⁸ Malashevich A and Vanderbilt D 2008 *Phys. Rev. Lett.* **101** 037210
- ³⁹ Raetz S, *et al.* 2019 *Phys. Rev. B.* **99** 224102
- ⁴⁰ Kuriakose M, *et al.* 2017 *Phys. Rev. B.* **96** 134122
- ⁴¹ Krukau A V, Vydrov O A, Izmaylov A F and Scuseria G E 2006 *J. Chem. Phys.* **125** 224106
- ⁴² J. Paier J, Marsman M, Hummer K, Kresse G, Gerber I C and Ángan J G 2006 *J. Chem. Phys.* **124** 154709
- ⁴³ Kim T-S, Kim Y-S, Hummer K and Kresse G 2009 *Phys. Rev. B.* **80** 035203
- ⁴⁴ Trepakov V A, *et al.* 2016 *arXiv e-prints* 1604.02428
- ⁴⁵ Ruello P, Pezeril T, Avanesyan S, Vaudel G, Gusev V, Infante I C, and Dkhil B 2012 *Appl. Phys. Lett.* **100** 212906
- ⁴⁶ Mason W P 1954 *Phys. Rev. B.* **96** 302
- ⁴⁷ Nieves P, Arapan S, Zhang S H, Kadzielawa A P, Zhang R F and Legut D 2020 *arXiv e-prints* 2009.01638
- ⁴⁸ Meier D, Aliouane N, Argyriou D N, Mydosh J A and Lorenz T 2007 *New Journal of Physics* **9** 100
- ⁴⁹ Fritsch D and Ederer C 2012 *Phys. Rev. B.* **86** 014406

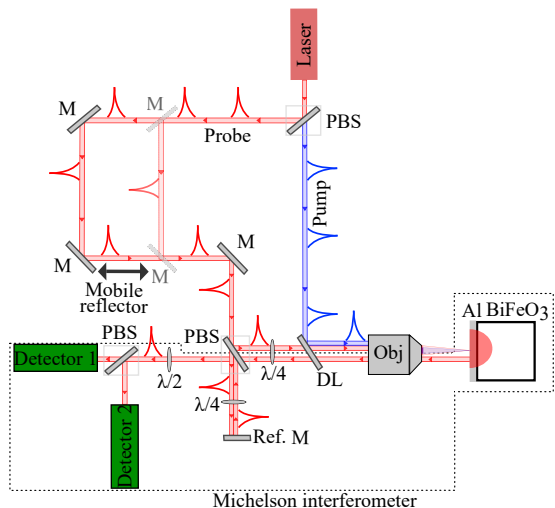


FIG. 5: Sketch of the experimental setup with first the pump focused (obj is an objective) on TbMnO_3 capped with an Al thin film, second the probe path (PBS polarized beam splitters, M are mirrors) and the mobile reflector for the time delay, third the detection path and the Michelson interferometer to detect the perpendicular surface displacements (two detectors are used to servo-control the Michelson and also to measure the phase of the reflectivity change).

I. DETAILS OF THE EXPERIMENTAL SETUP

For our pump-probe experiment as shown in Fig.5, a mode-locked Ti:sapphire (MAI TAI Spectra) laser source operating at 800 nm was used to thermally excite and optically detect the propagating acoustic modes in TbMnO_3 . The pulse duration is 200 fs and the pulse repetition rate is 80 MHz. In order to get some above band gap excitation, the TbMnO_3 sample was excited by light obtained from second harmonic generation (SHG) with wavelength 400 nm performed by doubling the pump frequency with a nonlinear crystal (BBO). The power of the two beams is fixed at $300 \mu\text{W}$. Acoustic measurements were performed using a standard stabilized Michelson interferometer sensitive to the perpendicular surface displacement. A 12 ns maximum pump-probe time delay is achieved using a mobile reflector mounted on a translation stage. Both the pump and probe beams are focused with a microscope objective with a numerical aperture of 0.9, fixed on a piezoelectric stage. A tilting system of the probe allows the mapping of acoustic waves propagating in any direction, thus providing information on the elastic properties of TbMnO_3 single crystals.

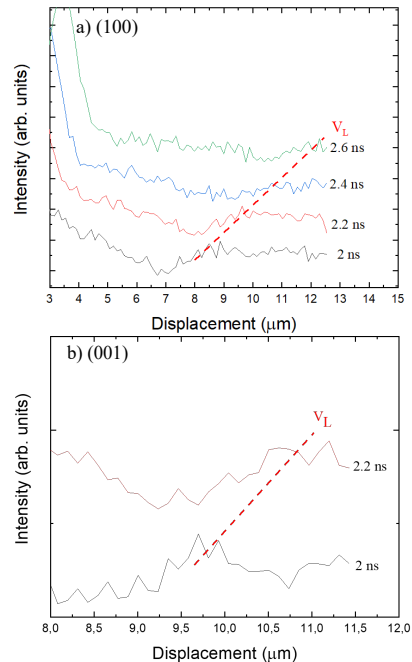


FIG. 6: Relative phase change of the electromagnetic field of the probe beam as a function of the displacement and at different probe time delay, along analyzed directions: (a) "2" and (b) "7".

II. MEASUREMENT OF THE LONGITUDINAL VELOCITY V_L

Figure 6 represents an enlargement of Fig. 2 in the article over the range of the longitudinal velocity V_L .

III. BULK WAVES SOUND VELOCITIES BY SOLVING THE CHRISTOFFEL EQUATIONS

We provide first the equations connecting the sound velocities of bulk waves to the C_{ij} elastic constants for each high symmetry planes $[x_2, x_3]$, $[x_1, x_3]$ and $[x_1, x_2]$.

In the $Pnma$ representation (**a**, **b**, **c**) of TbMnO_3 with angles $\alpha = \beta = \gamma = 90^\circ$, the symmetry of the elastic constant tensor is orthorhombic with 9 independent elastic constants:

$$C_{\mathbf{a},\mathbf{b},\mathbf{c}} = \begin{pmatrix} C_{11} & C_{12} & C_{13} & 0 & 0 & 0 \\ C_{12} & C_{22} & C_{23} & 0 & 0 & 0 \\ C_{13} & C_{23} & C_{33} & 0 & 0 & 0 \\ 0 & 0 & 0 & C_{44} & 0 & 0 \\ 0 & 0 & 0 & 0 & C_{55} & 0 \\ 0 & 0 & 0 & 0 & 0 & C_{66} \end{pmatrix} \quad (1)$$

The propagation of a bulk acoustic wave is described by Christoffel's equation :

$$\rho \frac{\partial^2 \vec{u}}{\partial t^2} = \vec{\nabla} \sigma \quad (2)$$

with ρ the volumic mass, $\vec{u} = \vec{u}_0 e^{i(\vec{k}\vec{r} - \omega t)}$ the displacement vector where \vec{k} is the wave vector, σ_i is the stress tensor equal to $C_{ij}\epsilon_j$, ϵ being the deformation tensor. The phase speed is defined by : $V = \frac{\omega}{k}$. All following analytical results were checked by a fully numerical resolution using the program "Christoffel" provided in Refs. 1,2 and agree with relations derived by Tsvankin.³

Equation 2 can be written in the following form:

$$\begin{pmatrix} u_1 \\ u_2 \\ u_3 \end{pmatrix} = \begin{pmatrix} C_{11}n_1^2 + C_{66}n_2^2 + C_{55}n_3^2 - \rho V^2 & (C_{12} + C_{66})n_1n_2 & (C_{13} + C_{55})n_1n_3 \\ (C_{12} + C_{66})n_1n_2 & C_{66}n_1^2 + C_{22}n_2^2 + C_{44}n_3^2 - \rho V^2 & (C_{23} + C_{44})n_2n_3 \\ (C_{13} + C_{55})n_1n_3 & (C_{23} + C_{44})n_2n_3 & C_{55}n_1^2 + C_{44}n_2^2 + C_{33}n_3^2 - \rho V^2 \end{pmatrix} \quad (3)$$

Here, \vec{n} is the unit vector in the slowness direction.

A. Propagation in the $[x_2, x_3]$ plane

If the wave vector lies in the $[x_2, x_3]$ plane, we can define $\vec{n}(0, \sin(\phi), \cos(\phi))$ with respect to the (\mathbf{c}) direction ($\phi = 0$). Then, equation 3 now reads:

$$\begin{pmatrix} u_1 \\ u_2 \\ u_3 \end{pmatrix} = \begin{pmatrix} C_{66}n_2^2 + C_{55}n_3^2 - \rho V^2 & 0 & 0 \\ 0 & C_{22}n_2^2 + C_{44}n_3^2 - \rho V^2 & (C_{23} + C_{44})n_2n_3 \\ 0 & (C_{23} + C_{44})n_2n_3 & C_{44}n_2^2 + C_{33}n_3^2 - \rho V^2 \end{pmatrix} \quad (4)$$

The solutions are for propagation in the $[x_2, x_3]$ plane:

1. a quasi-longitudinal mode polarized along (u_2, u_3) with speed equal to $V_L = V_+$,
2. a quasi-shear mode polarized along (u_2, u_3) and perpendicular to the quasi-longitudinal one, with speed equal to $V_{S1} = V_-$:

$$\rho V_{+/-}^2 = \frac{b \pm \sqrt{b^2 - 4c}}{2} \quad (5)$$

with

$$b = (C_{44} + C_{33})\cos^2(\phi) + (C_{44} + C_{22})\sin^2(\phi) \quad (6)$$

$$c = -[(C_{44} + C_{23})\cos(\phi)\sin(\phi)]^2 + (C_{44}\cos^2(\phi) + C_{22}\sin^2(\phi))(C_{33}\cos^2(\phi) + C_{44}\sin^2(\phi)) \quad (7)$$

3. a pure shear mode vertically polarized along (u_1) with a velocity V_{S2} :

$$\rho V_{S2}^2 = C_{66}\sin^2(\phi) + C_{55}\cos^2(\phi) \quad (8)$$

B. Propagation in the $[x_1, x_3]$ plane

If the wave vector lies in the $[x_1, x_3]$ plane, we can define $\vec{n}(\sin(\phi), 0, \cos(\phi))$ with respect to the (\mathbf{c}) direction ($\phi = 0$). Then, equation 3 now reads:

$$\begin{pmatrix} u_1 \\ u_2 \\ u_3 \end{pmatrix} = \begin{pmatrix} C_{11}n_1^2 + C_{55}n_3^2 - \rho V^2 & 0 & (C_{13} + C_{55})n_1n_3 \\ 0 & C_{66}n_1^2 + C_{44}n_3^2 - \rho V^2 & 0 \\ (C_{13} + C_{55})n_1n_3 & 0 & C_{55}n_1^2 + C_{33}n_3^2 - \rho V^2 \end{pmatrix} \quad (9)$$

The solutions are for propagation in the $[x_1, x_3]$ plane:

1. a quasi-longitudinal mode polarized along (u_1, u_3) with speed equal to $V_L = V_+$,
2. a quasi-shear mode polarized along (u_1, u_3) and perpendicular to the quasi-longitudinal one, with speed equal to $V_{S1} = V_-$:

$$\rho V_{+/-}^2 = \frac{b \pm \sqrt{b^2 - 4c}}{2} \quad (10)$$

with

$$b = (C_{55} + C_{33})\cos^2(\phi) + (C_{55} + C_{11})\sin^2(\phi) \quad (11)$$

$$c = -[(C_{55} + C_{13})\cos(\phi)\sin(\phi)]^2 + (C_{55}\cos^2(\phi) + C_{11}\sin^2(\phi))(C_{33}\cos^2(\phi) + C_{55}\sin^2(\phi)) \quad (12)$$

3. a pure shear mode vertically polarized along (u_2) with a velocity V_{S2} :

$$\rho V_{S2}^2 = C_{66}\sin^2(\phi) + C_{44}\cos^2(\phi) \quad (13)$$

C. Propagation in the $[x_1, x_2]$ plane

If the wave vector lies in the $[x_1, x_2]$ plane, we can define $\vec{n}(\sin(\phi), \cos(\phi), 0)$ with respect to the (\mathbf{b}) direction ($\phi = 0$). Then, equation 3 now reads:

$$\begin{pmatrix} u_1 \\ u_2 \\ u_3 \end{pmatrix} = \begin{pmatrix} C_{11}n_1^2 + C_{66}n_2^2 - \rho V^2 & (C_{12} + C_{66})n_1n_2 & 0 \\ (C_{12} + C_{66})n_1n_2 & C_{66}n_1^2 + C_{22}n_2^2 - \rho V^2 & 0 \\ 0 & 0 & C_{55}n_1^2 + C_{44}n_2^2 - \rho V^2 \end{pmatrix} \quad (14)$$

The solutions are for propagation in the $[x_1, x_2]$ plane:

1. a quasi-longitudinal mode polarized along (u_1, u_2) with speed equal to $V_L = V_+$,
2. a quasi-transverse mode polarized along (u_1, u_2) and perpendicular to the quasi-longitudinal one, with speed equal to $V_{S1} = V_-$:

$$\rho V_{+/-}^2 = \frac{b \pm \sqrt{b^2 - 4c}}{2} \quad (15)$$

with

$$b = (C_{66} + C_{22})\cos^2(\phi) + (C_{66} + C_{11})\sin^2(\phi) \quad (16)$$

$$c = -[(C_{66} + C_{12})\cos(\phi)\sin(\phi)]^2 + (C_{66}\cos^2(\phi) + C_{11}\sin^2(\phi))(C_{22}\cos^2(\phi) + C_{66}\sin^2(\phi)) \quad (17)$$

3. a pure shear mode vertically polarized along (u_3) with a velocity V_{S2} :

$$\rho V_{S2}^2 = C_{55}\sin^2(\phi) + C_{44}\cos^2(\phi) \quad (18)$$

D. Propagation along the $\langle 100 \rangle$ directions and time-domain Brillouin scattering experiments

For a wave vector and polarization along the $[100]$, $[010]$ and $[001]$ directions, the solutions are simple and enable selective determination of one elastic constant C_{ii} ($i=1..6$):

1. a shear mode with speed (V_S) such that $\rho V_S^2 = C_{66}$ [100][010], C_{44} [010][001], C_{55} [001][100], first and second direction being the propagation and polarization direction, respectively;
2. a longitudinal mode polarized according to (u_i) ($i=1..3$) with a velocity V_L :

$$\rho V_L^2 = C_{ii} \quad (19)$$

We have performed time-domain Brillouin scattering on TbMnO₃ single crystal along these three high sym-

metry directions.

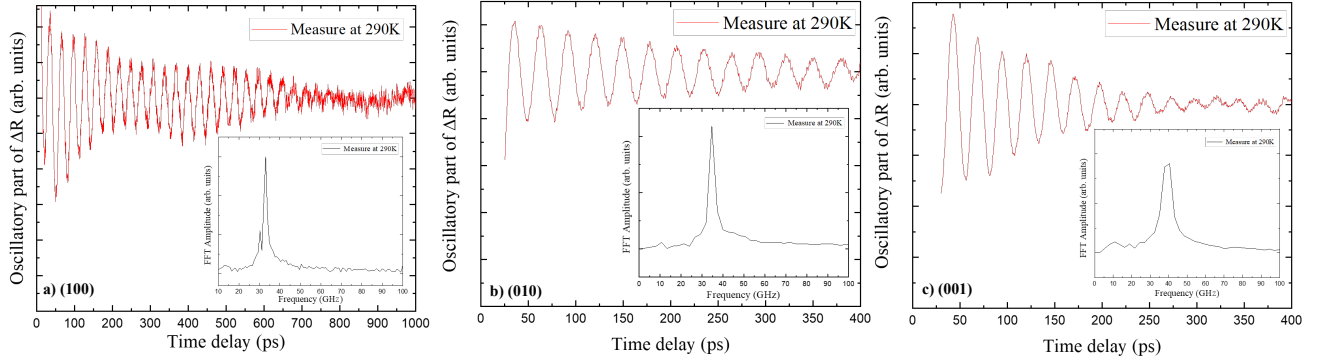


FIG. 7: Fast Fourier transform of Brillouin oscillations detected along the three high symmetry directions.

Figure 7 shows the Fast Fourier transform of the oscillations observed in the time resolved optical reflectivity of (100), (010) and (001) oriented single crystal (Pnma reference frame). For (100) investigated plane, one doublet is revealed at 30.25 GHz and at 32.97 GHz, measuring nV_L for two distinct orthogonal polarization of the electric field having two different values of refractive index n , in the range $[n_b, n_c]$. They correspond to the longitudinal (L) acoustic mode. The doublets arise from the birefringence in this (100) anisotropic plane, that we estimated to be $n_c - n_b \approx 0.08$ from our DFT calculations using hybrid HSE06 functional.

In the back-scattering configuration used in our experiment, the momentum conservation is obtained for $\vec{q}_{ac} = 2\vec{k}_{op}$ with \vec{q}_{ac} the momentum of acoustic phonon and \vec{k}_{op} the momentum of photon inside TbMnO₃. $k_{op} = 2\pi n / \lambda$ where λ is the wavelength of the laser probe and n is the averaged refractive index of TbMnO₃ at the wavelength λ . The phonon dispersion law is assumed to be written as $2\pi f_{ac} = V q_{ac}$ where V is the sound velocity in TbMnO₃ associated to the Brillouin frequency f_{ac} . As an example, we can thus deduce the velocity of the longitudinal wave (V_L) along [100] direction from Fig. 7

a using $\lambda = 813$ nm and our DFT calculated $n_b = 2.16$ and $n_c = 2.26$ and then C_{11} elastic constant:

$$V_L = 5693 - 5930 \text{ m.s}^{-1} \quad C_{11} = 257 \pm 10 \text{ GPa} \quad (20)$$

One should notice that our refractive index values (Pnma representation) are lower than the experimental low temperature (< 50 K) refractive index $n_b = 2.35^4$ (photon energy 2.5 eV, $\lambda = 496$ nm) and the theoretical one, $n_c = 2.7$ derived by Lu *et al.*⁵ from DFT GGA+U(3eV). Contrary to our approach, the time-domain Brillouin scattering allows only to measure few directions around the normal direction and necessitates additional crystal with different orientations for further scrutinizing elastic properties.

In Table III of the article, the measured longitudinal sound velocities measured by TDBS and the deduced C_{11} , C_{22} and C_{33} elastic constants show a reasonable agreement within 10%, 25% and 3% with DFT ones from Table II, respectively.

Nevertheless, it cannot be excluded that, if one consider the optical anisotropic character evidenced in ellipsometry measurements of Trepakov *et al.*,⁴ C_{22} elastic

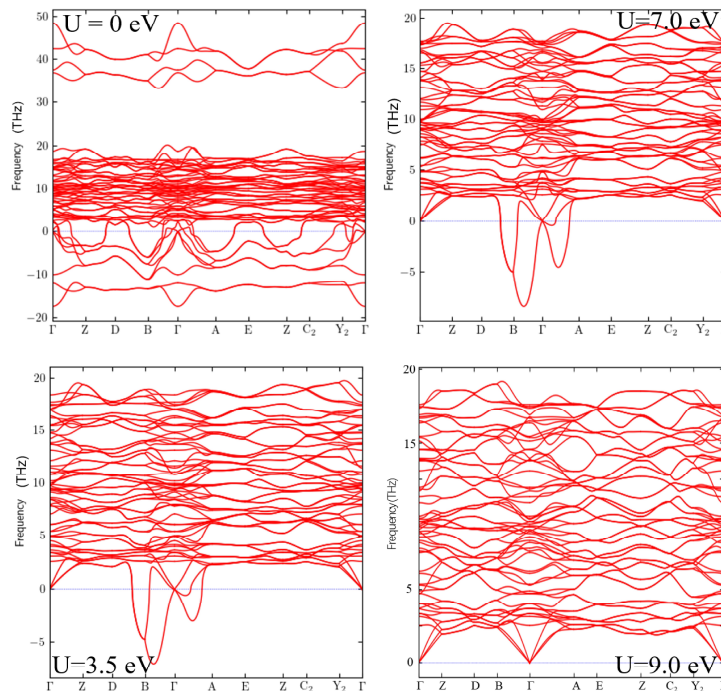


FIG. 8: Phonons spectra of TbMnO₃ calculated for four on-site Coulomb interaction U (0, 3.5, 7 and 9 eV) using GGA-PBESol exchange-correlation functional.

constant reported in Table III is probably 20 % overestimated because of used 10 % undervalue of low temperature (30K) n_a or n_c (hence, sound velocity) in the TDBS experiment analysis. Indeed, $n(T)$ dependence is expected to have the most general case of positive thermo-optic effect ($dn/dT > 0$) with higher refractive index values at room temperature (300K). Then, an overall agreement is plausible between out-of-plane and in-plane sound velocities, and elastic constants assessments. In the present work, these two approaches are found to be complementary as in-plane experiments did not evidenced propagating longitudinal wave within all high symmetry planes otherwise only a weak signal.

Among the off-diagonal elastic constants, only C_{23} could be measured thanks to longitudinal sound velocity along the bisecting direction $[x_2, x_3]$ (direction 2) and agrees within 13% with DFT one. Unfortunately, the longitudinal or the shear horizontal (S1) waves were not observed for those bisecting directions $[x_1, x_3]$ and $[x_1, x_2]$ which are necessary to assess selectively the two last elastic constants C_{13} and C_{12} .

IV. DYNAMICAL STABILITY

In this part, we have studied the dynamical stability versus U parameter performing phonons spectrum calculations using GGA-PBESol exchange-correlation functional and on-site Coulomb interaction for four U values (0, 3.5, 7 and 9 eV). As shown in Fig.8, dynamical stability is expected above $U=7$ eV which exhibits two negative frequencies near the Brillouin-zone center, while phonons frequencies are all positive in case of $U=9$ eV. This result is in good agreement with the fact, that we reach experimental band gap and atomic volume for $U \approx 7$ eV and GGA-PBESol exchange-correlation functional.

V. REFERENCES

* corresponding author : maximilien.cazayous@u-paris.fr

¹ Jaeken J W and Cottenier S 2016 *Computer Physics Com-*

- munications* **207** 445
- ² Jaeken J W and Cottenier S 2016 *Mendeley Data*) doi: 10.17632/4z25ff88c4.1
- ³ Tsvankin I 1997 *Geophysics* **62** 1292
- ⁴ Trepakov V A Dejneka A G Kvyatkovskii O E, Khvostova D, Potucek Z, Savinov M E, Jastrabik L, Wang X and Cheong S W 2016 *arXiv.cond-mat.mtrl-sci* 1604.02428
- ⁵ Lu-Gang C, Fa-Min L and Wen-Wu Z 2010 *Chinese Physics B* **19** 097101